



Magnetic excitations and absence of charge order in the van der Waals ferromagnet $\text{Fe}_{4.75}\text{GeTe}_2$



V. K. Bhartiya¹✉, T. Kim¹, J. Li¹, T. P. Darlington², D. J. Rizzo², Y. Gu¹, S. Fan¹, C. Nelson¹, J. W. Freeland³, X. Xu⁴, D. N. Basov², J. Pelliciani¹, A. F. May⁵, C. Mazzoli¹ & V. Bisogni¹✉

Understanding the ground state of van der Waals (vdW) magnets is crucial for designing devices leveraging these platforms. Here, we investigate the magnetic excitations and charge order in $\text{Fe}_{4.75}\text{GeTe}_2$, a vdW ferromagnet with ≈ 315 K Curie temperature. Using Fe L_3 -edge resonant inelastic X-ray scattering, we observe a dual nature of magnetic excitations, comprising a coherent magnon and a broad non-dispersive continuum extending up to 150 meV, 50% higher than in $\text{Fe}_{2.72}\text{GeTe}_2$. The continuum intensity is sinusoidally modulated along the stacking direction L , with a period matching the inter-slab distance. Our results indicate that while the dual character of the magnetic excitations is generic to Fe-Ge-Te vdW magnets, $\text{Fe}_{4.75}\text{GeTe}_2$ exhibits a longer out-of-plane magnetic correlation length, suggesting enhanced 3D magnetic character. Furthermore, resonant X-ray diffraction reveals that previously reported $\pm(1/3, 1/3, L)$ peaks originate from crystal structure rather than from charge order.

The discovery of ferromagnetism in two-dimensional van der Waals (vdW) ferromagnets has opened exciting frontiers in quantum matter research^{1–3}. In this context, the ternary Fe-Ge-Te vdW materials, such as Fe_3GeTe_2 and Fe_5GeTe_2 , hosting high-temperature long-range ferromagnetic order down to the two-dimensional (2D) structural limit, is a unique platform where miniaturized spintronics devices have already been proposed^{4–14}. In addition, strong electronic correlations are reported to drive these systems towards exotic ground states, that is, the heavy Fermions/Kondo physics^{15,16}, charge order (CO)¹⁷, flat bands¹⁸, optical anomalous hall effect (AHE)¹⁹, and orbital selective Mott transition (OSMT)²⁰.

Fe_3GeTe_2 ($150 < T_C < 230$ K) is the most thoroughly investigated member of the ternary Fe-Ge-Te vdW magnets. One of the intriguing findings is the coexistence of low energy coherent magnetic excitations (magnons) and a dispersionless non-Stoner-type continuum at higher energies^{16,20,21}. This dual character of magnetic excitations is beyond the framework of the linear spin wave theory, invoking the OSMT scenario—atypical to 3d transition metals—to explain the experimental observations²⁰. Are these dual magnetic excitations, a generic feature of the ternary Fe-Ge-Te vdW materials? If so, how do these excitations evolve with T_C ?

$\text{Fe}_{4.75}\text{GeTe}_2$ with the highest $T_C \approx 315$ K among Fe-Ge-Te 2D vdW ferromagnetic materials is an ideal member to investigate these questions. Moreover, it hosts the long-range ferromagnetic order remarkably close to

room temperature ≈ 270 K in the 2D structural limit^{4–6,8}. Deciphering the mechanism behind these high-temperature 2D vdW ferromagnets is essential to engineer novel heterostructures from 2D layers. However, despite enormous progress in understanding transport, magnetic, and structural properties of $\text{Fe}_{5-x}\text{GeTe}_2$ ^{4–6}, to date, the character of the magnetic excitations, their energy scale, and dimensionality remain unexplored in this material. The inelastic neutron scattering (INS) is a standard technique to address these issues^{22,23}, but the small size of the $\text{Fe}_{4.75}\text{GeTe}_2$ single crystals poses a challenge. Furthermore, a recent angular resolved photoemission spectroscopy (ARPES) and scanning tunneling microscopy (STM) study reports a CO¹⁷, that is shown to compete with the magnetic ordering. However, a bulk-sensitive signature of the CO, its electronic character and propagation vector are unexplored so far.

Here we present an investigation of the magnetic excitations and CO in $\text{Fe}_{4.75}\text{GeTe}_2$. To elucidate the character, energy scale, and dimensionality of the magnetic excitations, we employed high-resolution Fe L_3 -edge resonant inelastic X-ray scattering (RIXS) on a mm-sized single crystal $\text{Fe}_{4.75}\text{GeTe}_2$. RIXS complements INS to probe collective spin excitations and, in addition, can measure small sample volumes²⁴ easily accessing the high-energy spectral range where the thermal neutron flux is heavily reduced. Our findings suggest that $\text{Fe}_{4.75}\text{GeTe}_2$ hosts dual character of magnetic excitations, similarly to $\text{Fe}_{2.72}\text{GeTe}_2$, and despite being a 2D system structurally, it

¹National Synchrotron Light Source II, Brookhaven National Laboratory, Upton, NY, USA. ²Department of Physics, Columbia University, New York, New York, NY, USA. ³Advanced Photon Source, Argonne National Laboratory, Lemont, IL, USA. ⁴Department of Physics, University of Washington, Seattle, WA, USA. ⁵Materials Science and Technology Division, Oak Ridge National Laboratory, Oak Ridge, TN, USA. ✉e-mail: vbhartiya1@bnl.gov; bisogni@bnl.gov

displays a significant three-dimensional (3D) interaction between Fe-Ge-Te slabs that are ~ 10 Å apart. To investigate the bulk and electronic character of the proposed CO, we used synchrotron X-ray diffraction (XRD) and Fe K -edge resonant elastic X-ray scattering (REXS)^{25–27}. Our results demonstrate that the observed $\pm(1/3, 1/3, L)$ peaks are of structural origin, suggesting a doubling of structural unit cell along the c -axis. Overall, our work advances the current understanding of the magnetic properties of $\text{Fe}_{4.75}\text{GeTe}_2$ and shed light onto the whole family of Fe-Ge-Te vdW magnets.

The high-quality quenched single crystal of $\text{Fe}_{4.75}\text{GeTe}_2$ used for this study originated from the same batch as in refs. 4,28, which suggested similar magnetic properties for nominal composition ranging from $\text{Fe}_{4.7}\text{GeTe}_2$ to $\text{Fe}_{6.0}\text{GeTe}_2$. Figure 1a shows the rhombohedral unit cell of $\text{Fe}_{4.75}\text{GeTe}_2$ ($R\bar{3}m$ No. 166, $a = b \approx 4.04$ Å, $c \approx 29.19$ Å), characterized by three distinct Fe-Ge-Te slabs separated by ~ 10 Å. Within each slab, the Fe and Ge atoms occupy interior positions, while the Te atoms occupy the external positions. It develops ferromagnetic order below $T_C \approx 315$ K with magnetic moment pointing along the c -axis⁴.

For the X-ray absorption spectroscopy (XAS) and RIXS studies, the $\text{Fe}_{4.75}\text{GeTe}_2$ single crystal was oriented with (1 0 0) and (0 0 1) in the scattering plane, see Fig. 1b. The sample was cleaved in air with scotch tape just before loading it into the vacuum chamber. Figure 1c shows the XAS measured in the total electron yield (TEY) mode at 70 K. The observed L_3

and L_2 absorption peaks are in agreement with literature²⁹, supporting the high quality of the sample. The XAS data was used to identify the resonant energy for the RIXS study. To reduce the elastic scattering signal in the RIXS measurements, we used π -polarized incoming X-rays. The same sample was used for both REXS and XRD experiments, and it was aligned using an out-of-plane and two in-plane nuclear reflections.

The momentum transfer $\mathbf{Q}(HKL)$ associated with the RIXS spectra and the diffraction data are expressed in reciprocal lattice units ($4\pi/\sqrt{3}a4\pi/\sqrt{3}a2\pi/c$). The in-plane and out-of-plane momentum coverage was achieved by rotating both the scattering angle Ω and the X-rays incident angle θ . Extensive momentum coverage was achieved for the XRD experiment (2 keV of photon energy) and for the Fe K -edge REXS (≈ 7 keV of photon energy). For Fe L_3 -edge RIXS (≈ 710 eV of photon energy), we could span a large portion of the \mathbf{Q} -space in the L direction across several Brillouin zone (BZ) and up to $L = 3.23$ ($2\pi/c$), thanks to the large c -axis (≈ 29.19 Å) of the $\text{Fe}_{4.75}\text{GeTe}_2$, while in-plane we could cover up to $H_{\text{max}} = -0.35(4\pi/\sqrt{3}a)$ within the first BZ.

Results and discussion

Magnetic excitations in $\text{Fe}_{4.75}\text{GeTe}_2$

In the following two sections, we describe the investigation of the magnetic excitations and their momentum dependence in $\text{Fe}_{4.75}\text{GeTe}_2$ using Fe L_3 -

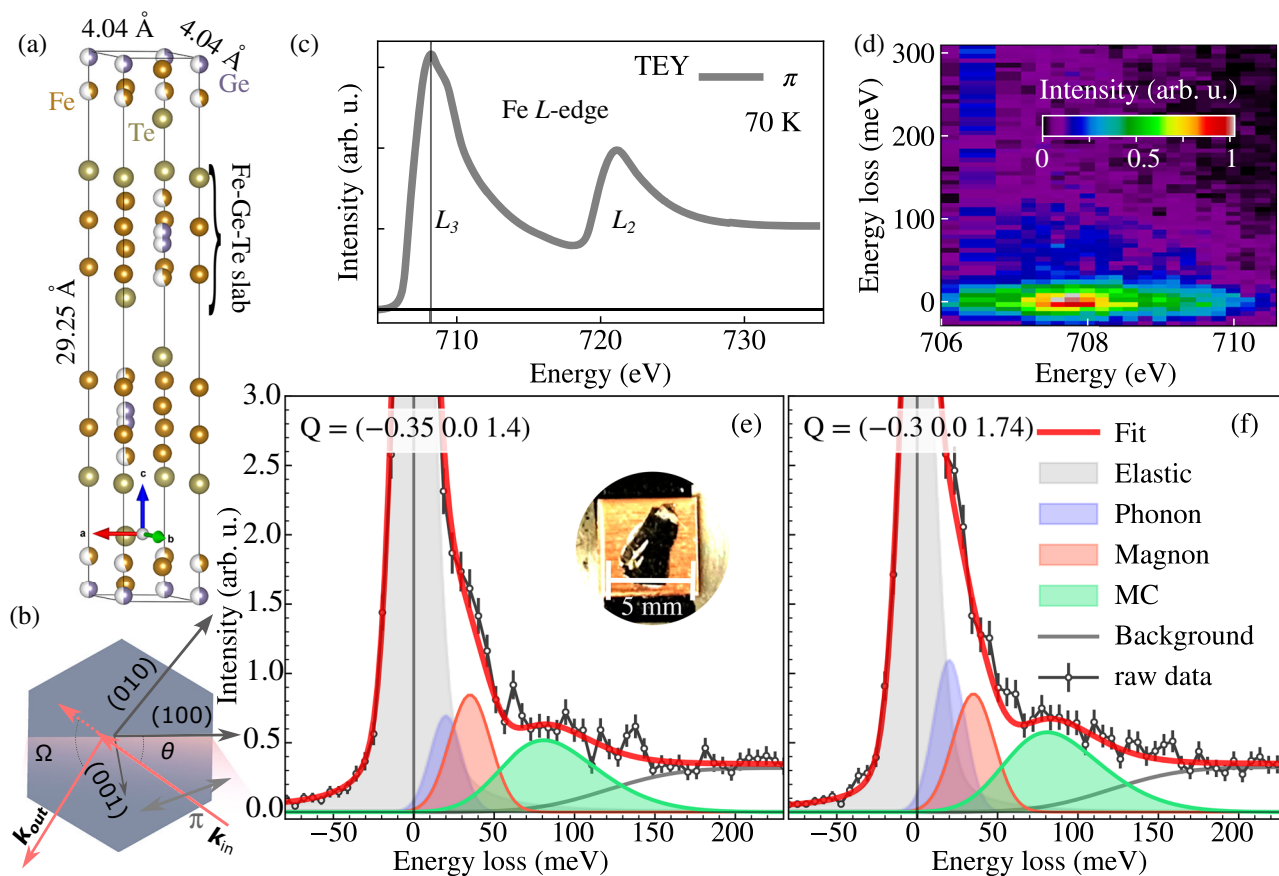


Fig. 1 | Magnetic excitations in the Fe L_3 -edge RIXS spectra of $\text{Fe}_{4.75}\text{GeTe}_2$. **a** $\text{Fe}_{4.75}\text{GeTe}_2$ crystal structure drawn using VESTA³⁴. A single unit cell contains three Fe-Ge-Te slabs. **b** Schematic of RIXS experimental geometry. In the hexagonal structure representation, two orthogonal wave vectors—(100) and (001)—form the scattering plane highlighted in pink. θ is an angle between the incident X-ray and the (100) axis while Ω is the scattering angle between incoming and outgoing X-ray. The double-headed arrow represents the π polarization of the incident light. **c** Fe $L_{3,2}$ -edge XAS measured at $\theta = 15^\circ$ in total electron yield (TEY) mode at 70 K. A solid vertical line represents the Fe L_3 -edge maximum, that corresponds to the incident photon energy (707.9 eV) used for the RIXS spectra. **d** RIXS intensity map measured

as a function of incident photon around the Fe L_3 -edge, and zoomed in to cover excitations below 300 meV. For this dataset, $\theta = 20^\circ$ and $\Omega = 95^\circ$ corresponding to $\mathbf{Q} = (-0.16, 0, 2.17)$. **e, f** Two representative RIXS scans (black dotted line) at $(-0.35, 0, 1.4)$ and $(-0.3, 0, 1.74)$. The low-energy excitations are fitted with an elastic peak (gray), a phonon (blue), a magnon (red), a broad continuum, and a background (gray line) stretching to higher energies. The red solid line represents the fit sum. The inset in (e) shows the measured $\text{Fe}_{4.75}\text{GeTe}_2$ single crystal. All RIXS spectra displayed in this work were measured at $T = 70$ K, using π polarization. The error bars of the RIXS spectra are defined assuming a Poisson distribution of the single-photon counted events.

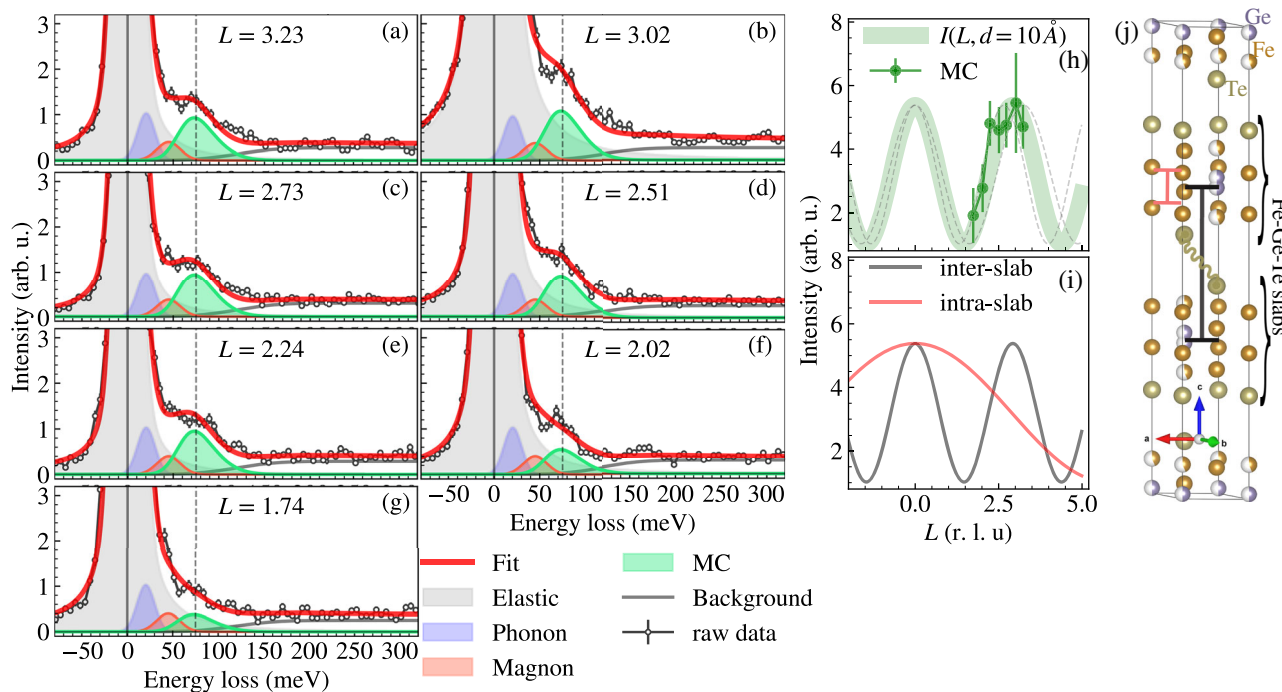


Fig. 2 | ***L* – dependent study of the magnetic continuum in $\text{Fe}_{4.75}\text{GeTe}_2$.** a–g RIXS spectra measured at different *L* values from 1.74 to 3.23 r.l.u., at 70 K. For all spectra, $H < |0.04|$ and $K = 0$. Each spectrum is fitted with an elastic peak (gray), a phonon (blue), a magnon (red), and a continuum (green), as introduced in Fig. 1e, f. The vertical dashed line marks the continuum centers around ~75 meV. h *L*-dependence of the continuum integrated spectral weight (green dotted line). The error bars are

half of one standard deviation. The thick green line is a sinusoidal fit of the data using Eq. (1) for $d = 10 \text{ \AA}$, while the dotted lines represent the upper and lower boundaries considering the extracted fit error for d of $\pm 1 \text{ \AA}$. i Calculated intensity modulation for intra-slab (red) and inter-slab (black) distances, as defined within the crystal structure displayed in (j) using with the same color convention. A gold curved line in (j) highlights the Te–Te distance across two neighboring slabs.

edge RIXS, and we discuss the results in comparison $\text{Fe}_{2.72}\text{GeTe}_2$ ^{16,20,30}. Figure 1d presents a RIXS intensity map measured as a function of incident photon energy across the Fe L_3 -edge. Although most of the spectral weight goes into high-energy fluorescence as expected for a metal (see Supplementary Fig. 2)²⁴, a weak component stretches from 0 up to ~150 meV resonating at the Fe L_3 peak. By fixing the incident photon energy to the maximum of the Fe L_3 resonance, we measured high-resolution RIXS spectra as a function of momentum transfer **Q**.

Figure 1e, f show RIXS spectra at two representative **Q** points with largest in-plane momentum components, **Q** = (−0.35 0 1.4) and (−0.3 0 1.74). We make use of both RIXS spectra to establish a minimum fitting model that describes the observed inelastic spectral weight below 200 meV. Details regarding the fitting and its procedure are reported in Supplementary Note 3. Taking $\text{Fe}_{2.72}\text{GeTe}_2$ as a reference case^{16,20}, we include in the fitting model a resolution limited phonon (blue peak), a magnon mode (red peak) due to spin-spin correlations between localized spins, and a broad magnetic continuum (green peak) coming from spin-spin interactions among itinerant electrons. We fix the phonon energy to 20 meV based on the room temperature Raman measurements presented in Supplementary Fig. 1 and consistently with²⁰. From the remaining spectral weight, we extract a magnon peak centered at $36 \pm 1 \text{ meV}$ and a continuum centered at $75 \pm 2 \text{ meV}$, extending up to ~150 meV. At higher energies, a background from the fluorescence tail dominates the spectral weight (gray solid line). While the magnetic continuum is peaked at twice the energy of the magnon, we exclude a dominant double magnon character, since this type of excitation is ~10 times weaker than the magnon^{31,32}. In our dataset, the continuum amplitude is comparable to the magnon, and its area is significantly larger than the latter, ruling out the double magnon character. While we cannot exclude the presence of double magnons in our data, their faint spectral weight would not impact the interpretation nor the extraction of the magnetic continuum.

For the spectra presented in Fig. 1e, f, we were not able to resolve any significant magnon dispersion given the proximity of the in-plane **Q**

components. However, a comparable magnon energy for similar momentum transfer has been reported for $\text{Fe}_{2.72}\text{GeTe}_2$ ^{16,20,30}, further supporting the nature of the ~36 meV peak. Similarly, the broad continuum peak (stretching up to 150 meV) resembles the one identified in $\text{Fe}_{2.72}\text{GeTe}_2$ ¹⁶, although in the latter system it extends only up to 100 meV. Based on these findings, we identify the low energy magnetic excitations in $\text{Fe}_{4.75}\text{GeTe}_2$ and assess the coexistence of the dual electron spin character in this system.

Our conclusion is underpinned by the INS studies of $\text{Fe}_{2.72}\text{GeTe}_2$ ^{16,20}. To explain this uncommon behavior in a 3d transition metal^{33–35}, an OSMT mechanism has been proposed for $\text{Fe}_{2.72}\text{GeTe}_2$ ²⁰, typically invoked in the context of strong multi-orbital correlations as realized by 4d/5d and *f* electron compounds^{36–39}. Within this scenario, it is possible to explain both the itinerant and the local magnetism manifesting in a multi-orbital system²⁰. Considering the emergence of giant Fe(3d)–Te(5p) and Fe(3d)–Ge(4s/4d) hybridization⁴⁰ and the flat bands^{18,41}, and the dual character of magnetic excitations evidenced by our study, the magnetic ground state of $\text{Fe}_{4.75}\text{GeTe}_2$ is likely governed by OSMT physics as well as in $\text{Fe}_{2.72}\text{GeTe}_2$. Theoretical validation would be valuable to confirm this aspect, requiring a comprehensive treatment of the strong multi-orbital correlations manifesting within such a complex crystal structure.

Origin of the magnetic continuum

Figure 2 shows the *L* dependent RIXS spectra along (0 0 *L*) from *L* = 1.74 r.l.u. to *L* = 3.23 r.l.u. In these measurements, we maximized the out-of-plane coverage by scanning mostly along (0 0 *L*), while minimizing the in-plane momentum transfer, e.g., $H < |0.04|$ r.l.u. and $K = 0$ r.l.u. A clear continuum peak emerges from all spectra, see Fig. 2a–g, and its position remains mostly invariant versus *L* as marked by a vertical dashed line. The dispersionless nature of the continuum agrees with the $\text{Fe}_{2.72}\text{GeTe}_2$ findings¹⁶. To directly compare the absolute RIXS intensities as a function of *L* (or scattering geometries), all spectra reported here are normalized to integrated fluorescence peak and self-absorption corrected as described in Supplementary Note 2. Already from the raw data, the

continuum intensity appears to decrease for decreasing L . Note that while in $\text{Fe}_{2.72}\text{GeTe}_2$ the continuum is maximized around the in-plane BZ boundary¹⁶, here we find a significant spectral weight close to the in-plane BZ center.

The origin of the L -dependent intensity modulation of the continuum in $\text{Fe}_{2.72}\text{GeTe}_2$ was associated with the two Fe sites, yielding a characteristic length scale along the c -axis within Fe-Ge-Te slab¹⁶. The goal of this section is to extract this information for $\text{Fe}_{4.75}\text{GeTe}_2$. We fit the RIXS spectra in Fig. 2 using the model introduced in Fig. 1e, f. To effectively implement the fitting model, we made some key assumptions. Given the strong elastic line intensity and the unknown magnon dispersion for this material, we fixed the fitting parameters (peak position and width) of the lowest energy modes—phonon and magnon—to match the values extracted for $\mathbf{Q} = (-0.35\ 0\ 1.4)$ r.l.u. These assumptions are valid because the low-energy spectral weight (below 40 meV) only influences the elastic line shape and leaves the high-energy dispersionless continuum unaffected. This approach enabled us to utilize a consistent fitting model across all RIXS spectra. Regarding the fitting of the continuum itself, we fixed its position and width to reproduce the broad and dispersionless character of this excitation^{16,20}, while its amplitude was allowed to change. More details on the fitting procedure can be found in Supplementary Note 3. As a result of this analysis, we obtain the L -dependent evolution of the continuum intensity which follows a sinusoidal behavior, as highlighted in Fig. 2h. A comparison of the L -dependent magnetic continuum intensity with and without self-absorption correction is shown in Supplementary Fig. 3. The magnitude of intensity modulation is robust and independent of self-absorption correction.

When dealing with a continuum or a dispersionless excitation, the \mathbf{Q} -dependent modulation of its intensity or structure factor encodes the distance between the interacting atoms along the selected \mathbf{Q} -direction. Hard X-ray RIXS and INS—enabling a wide coverage of reciprocal space—have been extensively used to show the formation of new magnetic superstructures by monitoring the \mathbf{Q} -modulation of the spectral weight^{16,42,43}. Following these works, the frequency of the continuum structure factor modulation can be captured by a simple qualitative function:

$$I(L) \propto \cos(L \cdot d/2)^2, \quad (1)$$

where L is the momentum transfer vector and d is the real space inter-atomic distance along the c -axis within the unit cell. By fitting the data points displayed in Fig. 2h, we extract a distance of $d = 10 \pm 1$ Å.

In the case of $\text{Fe}_{2.72}\text{GeTe}_2$, the L -dependent INS structure factor of the continuum yielded an intra-slab distance $d \sim 2.7$ Å¹⁶. Such a length-scale corresponds to the Fe-Fe dumbbell (a dimer-like structure corresponding to the largest exchange interaction) superstructure oriented along the c -axis within an individual Fe-Ge-Te slab. This finding suggests that the magnetic continuum in $\text{Fe}_{2.72}\text{GeTe}_2$ originates from the quasi-molecular character of the magnetic states formed by the Fe-Fe dumbbell, and furthermore, it identifies the atoms and exchange path that contribute to the strongest magnetic exchange interaction in the system²⁰.

To identify the interacting atoms and exchange path behind the continuum intensity modulation in $\text{Fe}_{4.75}\text{GeTe}_2$, we display in Fig. 2i a simulation of $I(L)$ based on a representative intra-slab distance (red) and inter-slab distance (black). Such distances are highlighted in the unit cell of Fig. 2l, using the same color code. The intra-slab distance $d \sim 2.53$ Å connecting two Fe atoms within the same Fe-Ge-Te slab fails in reproducing the observed modulation, despite it well described the L -dependent continuum modulation for $\text{Fe}_{2.72}\text{GeTe}_2$ ¹⁶. Rather, we find that an inter-slab distance $d \sim 11$ Å connecting the center of two consecutive slabs well reproduces the continuum modulation for $\text{Fe}_{4.75}\text{GeTe}_2$. Our finding supports the presence of an inter-slab exchange path along the c -axis, suggesting a three-dimensional character for the magnetic interaction in $\text{Fe}_{4.75}\text{GeTe}_2$. Additionally, we identify the Fe-Ge-Te slabs as the interacting magnetic units in $\text{Fe}_{4.75}\text{GeTe}_2$. This is consistent with recent X-ray magnetic circular dichroism and ARPES studies underlining the key role of Te and Ge in determining the itinerant long-range ferromagnetism in $\text{Fe}_{4.75}\text{GeTe}_2$ ^{29,40}, owing to the strong

hybridization and covalent nature of the Fe-Te and the Fe-Ge bonds. Based on atomic position considerations, we suggest that the shorter Fe-Te nearest neighbor distance (2.63 Å) in $\text{Fe}_{4.75}\text{GeTe}_2$ with respect to $\text{Fe}_{2.72}\text{GeTe}_2$ (2.643 Å) possibly favors the inter-slab exchange mediated by the Te sites (highlighted by the curved line in Fig. 2j). Overall, we speculate that the inter-slab exchange interaction revealed by our study could be crucial for determining the high T_C in $\text{Fe}_{4.75}\text{GeTe}_2$, endorsed by recent studies on epitaxially grown thin films where T_C is found to be inversely proportional to the inter-slab distance⁴⁴.

Absence of charge order in bulk $\text{Fe}_{4.75}\text{GeTe}_2$

Recently, selected area electron diffraction studies⁴⁵ reported a superstructure modulation vector $\mathbf{Q}_1 = \pm 1/3\ (1\ 1\ 3)$ above 100 K, fading away at lower temperatures with a diffused line along $1/3\ (1\ 1\ L)$ together with a new $\mathbf{Q}_2 = \pm 3/10\ (0\ 0\ 3L)$ order. A short range $\sqrt{3}a \times \sqrt{3}a\ R30^\circ$ order was observed by single crystal XRD and the high-angle annular dark field image and associated with Fe occupancy of a crystallographic split-site⁴. Further STM and ARPES investigations¹⁷ confirmed the existence of a $\sqrt{3}a \times \sqrt{3}a\ R30^\circ$ in-plane periodic modulation and assigned it to the charge ordering. To further the understanding of the bulk signature, electronic character, and propagation vectors of \mathbf{Q}_1 and \mathbf{Q}_2 in $\text{Fe}_{4.75}\text{GeTe}_2$, in the following, we present synchrotron XRD (~ 2.1 keV) and REXS (Fe K -edge, ~ 7.1 keV) investigations.

We confirmed the in-plane order $\sqrt{3}a \times \sqrt{3}a\ R30^\circ$ in our $\text{Fe}_{4.75}\text{GeTe}_2$ single crystal by finding several symmetry-equivalent peaks at 150 K, as represented in Fig. 3a. Figure 3b reports the H , K , and L scans of a representative peak with $(1/3\ 1/3)$ in-plane components, measured using ~ 2.1 keV X-rays. Interestingly, we find that the out-of-plane component peaks at $L = 7.5$ r.l.u. No significant temperature dependence is detected for this peak while going across 100 K, as displayed in Fig. 3c. The extended L scan of $(2/3\ -1/3\ L)$ and $(1/3\ 1/3\ L)$ peaks are presented in Fig. 3d, using ~ 7.1 keV X-rays (dotted lines): a clear $(1/3\ 1/3\ 3n + 1.5)$ with $n = 0, 1, 2, 3, \dots$ periodicity emerges even at 7 K. The observed $(1/3\ 1/3\ 3n + 1.5)$ modulation differs from the previously reported $\pm 1/3\ (1\ 1\ 3)$ order⁴⁵ and is also distinct from the $(0\ 0\ 3n)$ selection rule expected for a rhombohedral unit cell (space group $R\bar{3}m$). For reference, we reproduce in Fig. 3(d) the $(0\ 0\ L)$ scan (gray line) showing the $(0\ 0\ 3n)$ periodicity of the structural Bragg peak. The satellite structure visible in the $(0\ 0\ L)$ scan is attributed to a second crystallite present in the sample. Also, no fingerprint of $\mathbf{Q}_2 = \pm 3/10\ (0\ 0\ 3L)$ is observed in our data down to 7 K.

The intensities of $(0\ 0\ L)$ and $(2/3\ -1/3\ L)$ or $(1/3\ 1/3\ L)$ scans cannot be directly compared in Fig. 3d, as we used a higher intensity detuning filter for the main structural Bragg peaks along $(0\ 0\ L)$. An absolute intensity comparison between $(1/3\ 1/3\ 22.5)$ and $(0\ 0\ 9)$ is presented in 3e, showing that the intensities of both peaks are of the same order of magnitude, with the $(0\ 0\ 9)$ peak $\sim 50\%$ stronger than $(1/3\ 1/3\ 22.5)$.

Additionally, using Fe K -edge REXS, we investigated the resonance effect of the $(1/3\ 1/3\ 22.5)$ peak. The resulting fixed- \mathbf{Q} energy scan is presented in Fig. 3e (green dotted line) and compared to the energy scan of the $(0\ 0\ 9)$ structural Bragg peak (gray line). Both scans present a similar behavior, with no resonance enhancement. The Fe K -edge XAS of $\text{Fe}_{4.75}\text{GeTe}_2$ is reproduced for reference in the same figure.

Overall, our REXS and XRD studies report the presence of a commensurate $(1/3\ 1/3\ L)$ Bragg peak with a $3n + 1.5$ out-of-plane modulation, no temperature dependence down to 7 K, and no resonance effect. Based on these observations, we propose these peaks originate from the crystal structure rather than CO^{25–27,46}. This conclusion is further corroborated by the comparable peak intensity with respect to main structural Bragg peaks. Furthermore, we underline that the observed $3n + 1.5$ out-of-plane periodicity is not compatible with the space group $R\bar{3}m$ proposed for $\text{Fe}_{4.75}\text{GeTe}_2$, instead, it infers doubling of structural unit cell along the c -axis and reduced crystal symmetry. One direct consequence of reduced lattice symmetry would be a more complex network of magnetic interactions, which might be crucial to interpret the various kinks in the magnetization versus temperature diagram⁴.

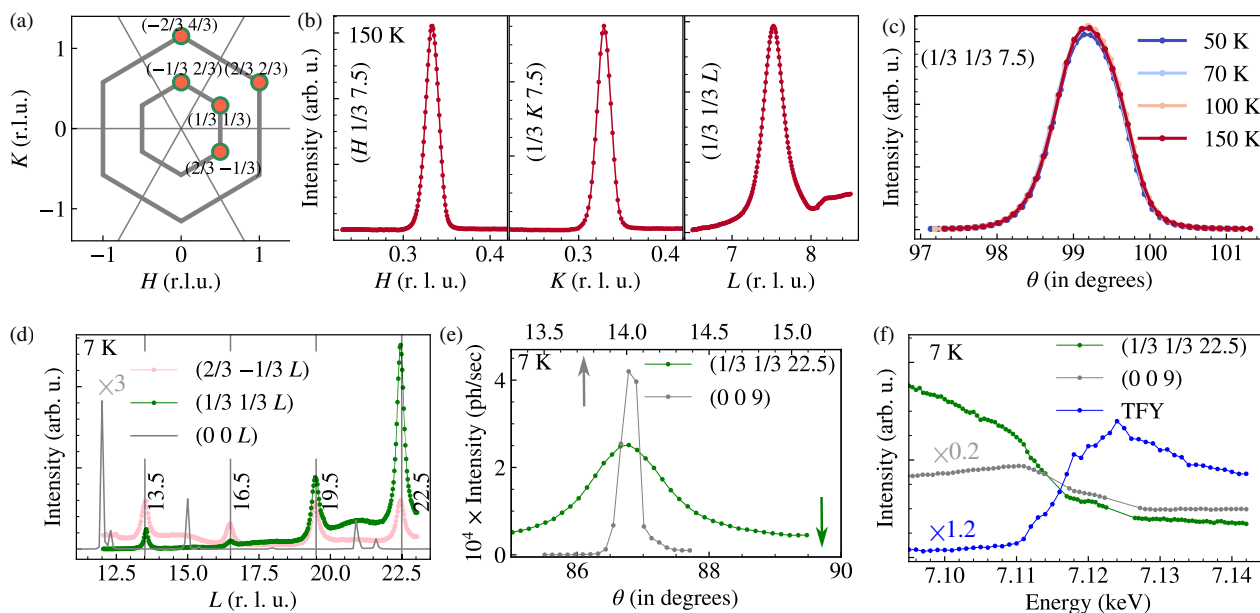


Fig. 3 | Investigation of charge order in $\text{Fe}_{4.75}\text{GeTe}_2$ by REXS and XRD. **a** A sketch highlighting the measured symmetry equivalent Q positions. **b** H , K , and L scans of a representative $(1/3\ 1/3\ 7.5)$ peak using 2.1 keV X-ray energy at 150 K. **c** The temperature dependence of the $(1/3\ 1/3\ 7.5)$ peak. **d** Fixed-energy Q -scan of $(1/3\ 1/3\ L)$ (green dotted line), $(2/3 -1/3\ L)$ (pink dotted line), and of $(0\ 0\ L)$ (gray line) along the L direction. The temperature was set to 7 K for this measurement and the X-ray

energy was tuned prior to the Fe K -edge, ~ 7.1 keV. Double peaks in $(0\ 0\ L)$ scan are due to a second crystallite. $(0\ 0\ L)$ scan is rescaled to match y-scale. **e** Absolute intensity comparison between $(1/3\ 1/3\ 22.5)$ and $(0\ 0\ 9)$ peaks. **f** Fixed- Q energy scan of $(1/3\ 1/3\ 22.5)$ (green dotted line) and $(0\ 0\ 9)$ (gray dotted line) peaks, rescaled to match y-scale. The Fe K -edge XAS of $\text{Fe}_{4.75}\text{GeTe}_2$ measured in total fluorescence yield (TFY) mode is displayed (rescaled) for reference (blue dotted line).

To reconcile the discrepancy between our observations and the ones reported in the literature^{17,45}, we should acknowledge intrinsic differences connected with the techniques involved. STM and ARPES mostly probe the surface, which in certain materials can significantly differ from the bulk^{47–50}. Electron diffraction instead probes the bulk, but the required sample preparation methods—such as focused ion beam and grinding—might introduce permanent micro-structural changes affecting the material response^{51,52}. Finally, we cannot exclude a sample-to-sample variation in determining the ultimate material properties. $\text{Fe}_{4.75}\text{GeTe}_2$ single crystals are known to have stacking faults and different samples (especially grown by different groups) might even have slightly different Fe concentration. To advance the understanding of this complex system, it would be helpful to perform on the same sample both surface-sensitive (STM, ARPES) and bulk-sensitive (XRD, REXS) investigations.

In summary, our work sheds light on the magnetic excitations in ferromagnet $\text{Fe}_{4.75}\text{GeTe}_2$. Using high-resolution RIXS at the Fe L_3 -edge, we reveal that $\text{Fe}_{4.75}\text{GeTe}_2$ hosts dual character of magnetic excitations composed of a magnon and a continuum, similarly to the more extensively characterized $\text{Fe}_{2.72}\text{GeTe}_2$, and prove that the dual character of magnetic excitation, known to be driven by OSMT, is common to ternary Fe-Ge-TevdW materials. The out-of-plane modulation of the continuum intensity reveals the presence of a strong out-of-plane inter-slab exchange path, where the interacting magnetic units are the neighboring Fe-Ge-Te slabs. We conclude that $\text{Fe}_{4.75}\text{GeTe}_2$ behaves like a 3D magnet, and we discuss this finding in connection to its T_C , the highest among Fe-Ge-TevdW materials. Additionally, employing XRD and REXS, we explored the bulk character, the electronic origin, and the propagation vector of the previously reported CO with $(1/3\ 1/3)$ in-plane components. The absence of temperature and resonance effects, and the commensurability with the crystal structure led us to conclude that the observed Bragg peaks do not originate from CO but rather crystal structure with reduced symmetry. The presence of the $(1/3\ 1/3\ 3n + 1.5)$ peaks suggests a doubling of the unit cell along the c -axis, indicating a subtle change in the stacking sequence or atomic positions that is not captured by the $R\bar{3}m$ space group.

Methods

X-ray absorption (XAS) and resonant inelastic X-ray scattering (RIXS)

High-resolution XAS and RIXS experiments were carried out at the SIX 2-ID beamline of NSLS-II⁵³. The experimental energy resolution at the Fe L_3 -edge (~ 708 eV) was 21 meV for the RIXS measurements, determined by the full width at half-maximum of the elastic peak measured from a reference multilayer sample. To suppress the elastic line, π polarization was used throughout the experiment.

Resonant elastic X-ray scattering (REXS) and X-ray diffraction (XRD)

Synchrotron-based XRD was used to measure the rocking curves and temperature dependence of $(1/3\ 1/3\ 7.5)$ peak at 29-ID beamline of APS, with a photon energy of 2.1 keV. The Fe K -edge REXS was performed at the 4-ID beamline of NSLS-II.

Raman spectroscopy

We performed room-temperature Raman scattering ($\lambda = 6328$ Å) on a $\text{Fe}_{4.75}\text{GeTe}_2$ flake exfoliated on SiO_2/Si and oriented as c -axis normal using a LabRAM HR Evolution Raman microscope from Horiba Scientific using 100×0.9 NA Olympus air objective. Spectra were recorded using an 1800 gr/mm holographic grating and Synapse II front-illuminated EMCCD (Supplementary Fig. 1).

Data availability

Data supporting the findings of this study are available from the corresponding author on reasonable request.

Received: 19 November 2024; Accepted: 7 July 2025;

Published online: 21 July 2025

References

- Burch, K. S., Mandrus, D. & Park, J. G. Magnetism in two-dimensional van der Waals materials. *Nature* **563**, 47–52 (2018).

2. Gibertini, M., Koperski, M., Morpurgo, A. F. & Novoselov, K. S. Magnetic 2D materials and heterostructures. *Nat. Nanotechnol.* **14**, 408–419 (2019).
3. Wang, Q. H. et al. The magnetic genome of two-dimensional van der Waals materials. *ACS Nano* **17**, 47 (2021).
4. May, A. F. et al. Ferromagnetism near room temperature in the cleavable van der Waals crystal Fe_5GeTe_2 . *ACS Nano* **13**, 57 (2019).
5. Zhang, H. et al. Itinerant ferromagnetism in van der Waals $\text{Fe}_{5-x}\text{GeTe}_2$ crystals above room temperature. *Phys. Rev. B* **102**, 64417 (2020).
6. Chen, H. et al. Above-room-temperature ferromagnetism in thin van der Waals flakes of cobalt-substituted Fe_5GeTe_2 . *ACS Appl. Mater. Interfaces* **15**, 3287–3296 (2023).
7. Wang, Z. et al. Tunneling spin valves based on $\text{Fe}_3\text{GeTe}_2/\text{hBN}/\text{Fe}_3\text{GeTe}_2$ van der Waals heterostructures. *Nano Lett.* **18**, 4303–4308 (2018).
8. Georgopoulou-Kotsaki, E. et al. Significant enhancement of ferromagnetism above room temperature in epitaxial 2d van der Waals ferromagnet $\text{Fe}_{5-x}\text{GeTe}_2/\text{Bi}_2\text{Te}_3$ heterostructures. *Nanoscale* **15**, 2223–2233 (2023).
9. Li, Q. et al. Patterning-induced ferromagnetism of Fe_3GeTe_2 van der Waals materials beyond room temperature. *Nano Lett.* **18**, 7 (2018).
10. Alghamdi, M. et al. Highly efficient spin-orbit torque and switching of layered ferromagnet Fe_3GeTe_2 . *Nano Lett.* **19**, 25 (2019).
11. Yang, M. et al. Highly enhanced Curie temperature in Ga-implanted Fe_3GeTe_2 van der Waals material. *Adv. Quantum Technol.* **3** (2020). <https://doi.org/10.1002/qute.202000017>
12. Ding, B. et al. Observation of magnetic skyrmion bubbles in a van der Waals ferromagnet Fe_3GeTe_2 . *Nano Lett.* **20**, 2023 (2020).
13. Wu, Y. et al. Néel-type skyrmion in $\text{WTe}_2/\text{Fe}_3\text{GeTe}_2$ van der Waals heterostructure. *Nat. Commun.* **11**, 1–6 (2020).
14. Deng, Y. et al. Gate-tunable room-temperature ferromagnetism in two-dimensional Fe_3GeTe_2 . *Nature* **563**, 94–99 (2018).
15. Zhang, Y. et al. Emergence of Kondo lattice behavior in a van der Waals itinerant ferromagnet, Fe_3GeTe_2 . *Sci. Adv.* **4**, eaao6791 (2018).
16. Bao, S. et al. Neutron spectroscopy evidence on the dual nature of magnetic excitations in a van der Waals metallic ferromagnet $\text{Fe}_{2.72}\text{GeTe}_2$. *Phys. Rev. X* **12**, 011022 (2022).
17. Wu, X. et al. Direct observation of competition between charge order and itinerant ferromagnetism in the van der Waals crystal $\text{Fe}_{5-x}\text{GeTe}_2$. *Phys. Rev. B* **104**, 165101 (2021).
18. Wu, H. et al. Reversible non-volatile electronic switching in a near-room-temperature van der Waals ferromagnet. *Nat. Commun.* **15**, 2739 (2024).
19. Kato, Y. D. et al. Optical anomalous hall effect enhanced by flat bands in ferromagnetic van der Waals semimetal. *npj Quantum Mater.* **7**, 73 (2022).
20. Bai, X. et al. Antiferromagnetic fluctuations and orbital-selective Mott transition in the van der Waals ferromagnet $\text{Fe}_{3-x}\text{GeTe}_2$. *Phys. Rev. B* **106**, L180409 (2022).
21. Xu, X. et al. Signature for non-stoner ferromagnetism in the van der Waals ferromagnet Fe_3GeTe_2 . *Phys. Rev. B* **101**, 201104 (2020).
22. Bettler, S. et al. Magnetic structure and spin waves in the frustrated ferro-antiferromagnet $\text{Pb}_2\text{VO}(\text{PO}_4)_2$. *Phys. Rev. B* **99**, 184437 (2019).
23. Bhartiya, V. K. et al. Inelastic neutron scattering determination of the spin Hamiltonian for $\text{BaCdVO}(\text{PO}_4)_2$. *Phys. Rev. B* **103**, 144402 (2021).
24. Pelliciani, J. et al. Tuning spin excitations in magnetic films by confinement. *Nat. Mater.* **20**, 188–193 (2021).
25. Abbamonte, P. et al. Crystallization of charge holes in the spin ladder of $\text{Sr}_{14}\text{Cu}_{24}\text{O}_{41}$. *Nature* **431**, 1078–1081 (2004).
26. Chen, X. M. et al. Remarkable stability of charge density wave order in $\text{La}_{1.875}\text{Ba}_{0.125}\text{CuO}_4$. *Phys. Rev. Lett.* **117**, 167001 (2016).
27. Shen, Y. et al. Charge condensation and lattice coupling drives stripe formation in nickelates. *Phys. Rev. Lett.* **126**, 177601 (2021).
28. May, A. F., Calder, S., Cantoni, C., Cao, H. & McGuire, M. A. Magnetic structure and phase stability of the van der Waals bonded ferromagnet $\text{Fe}_{3-x}\text{GeTe}_2$. *Phys. Rev. B* **93**, 14411 (2016).
29. Yamagami, K. et al. Enhanced d-p hybridization intertwined with anomalous ground state formation in the van der Waals itinerant magnet Fe_5GeTe_2 . *Phys. Rev. B* **106**, 45137 (2022).
30. Calder, S., Kolesnikov, A. I. & May, A. F. Magnetic excitations in the quasi-two-dimensional ferromagnet $\text{Fe}_{3-x}\text{GeTe}_2$ measured with inelastic neutron scattering. *Phys. Rev. B* **99**, 094423 (2019).
31. Li, J. et al. Single- and multimagnon dynamics in antiferromagnetic $\alpha\text{-Fe}_2\text{O}_3$ thin films. *Phys. Rev. X* **13**, 011012 (2023).
32. Elnaggar, H. et al. Magnetic excitations beyond the single- and double-magnons. *Nat. Commun.* **14**, 2749 (2023).
33. Xie, T. et al. Odd and even modes of neutron spin resonance in the bilayer iron-based superconductor $\text{CaKFe}_4\text{As}_4$. *Phys. Rev. Lett.* **120**, 267003 (2018).
34. Chen, X. et al. Unconventional Hund metal in a weak itinerant ferromagnet. *Nat. Commun.* **11**, 3076 (2020).
35. Song, Y. et al. High-energy magnetic excitations from heavy quasiparticles in CeCu_2Si_2 . *npj Quantum Mater.* **6**, 60 (2021).
36. Anisimov, V. I., Nekrasov, I. A., Kondakov, D. E., Rice, T. M. & Sigrist, M. Orbital-selective mott-insulator transition in $\text{Ca}_{2-x}\text{Sr}_x\text{RuO}_4$. *Eur. Phys. J. B* **25**, 191–201 (2002).
37. Kim, M. et al. Signature of Kondo hybridisation with an orbital-selective Mott phase in 4d $\text{Ca}_{2-x}\text{Sr}_x\text{RuO}_4$. *npj Quantum Mater.* **7**, 59 (2022).
38. de' Medici, L., Georges, A., Kotliar, G. & Biermann, S. Mott transition and Kondo screening in *f*-electron metals. *Phys. Rev. Lett.* **95**, 066402 (2005).
39. de' Medici, L., Hassan, S. R., Capone, M. & Dai, X. Orbital-selective Mott transition out of band degeneracy lifting. *Phys. Rev. Lett.* **102**, 126401 (2009).
40. Yamagami, K. et al. Itinerant ferromagnetism mediated by giant spin polarization of the metallic ligand band in the van der Waals magnet Fe_5GeTe_2 . *Phys. Rev. B* **103**, L060403 (2021).
41. Wang, F. & Zhang, H. Flat bands and magnetism in Fe_4GeTe_2 and Fe_5GeTe_2 due to bipartite crystal lattices. *Phys. Rev. B* **108**, 195140 (2023).
42. Revelli, A. et al. Fingerprints of Kitaev physics in the magnetic excitations of honeycomb iridates. *Phys. Rev. Res.* **2**, 43094 (2020).
43. Revelli, A. et al. Quasimolecular electronic structure of the spin-liquid candidate $\text{Ba}_3\text{InIr}_2\text{O}_9$. *Phys. Rev. B* **106**, 155107 (2022).
44. Silinskas, M. et al. Self-intercalation as origin of high-temperature ferromagnetism in epitaxially grown Fe_5GeTe_2 . *Phys. Rev. Lett.* **133**, 256702 (2024).
45. Gao, Y. et al. Spontaneous (anti)meron chains in the domain walls of van der Waals ferromagnetic $\text{Fe}_{5-x}\text{GeTe}_2$. *Adv. Mater.* **32**, 2005228 (2020).
46. Wu, S. et al. Discovery of charge order in the transition metal dichalcogenide Fe_xNbS_2 . *Phys. Rev. Lett.* **131**, 186701 (2023).
47. Brown, S. E., Fradkin, E. & Kivelson, S. A. Surface pinning of fluctuating charge order: an extraordinary surface phase transition. *Phys. Rev. B* **71**, 224512 (2005).
48. Gu, Q. et al. Detection of a pair density wave state in UTe_2 . *Nature* **618**, 921–927 (2023).
49. Kengle, C. S. et al. Absence of bulk charge density wave order in the normal state of UTe_2 . *Nat. Commun.* **15**, 9713 (2024).
50. Theuss, F. et al. Absence of a bulk thermodynamic phase transition to a density wave phase in UTe_2 . *Phys. Rev. B* **110**, 144507 (2024).
51. Mayer, J., Giannuzzi, L. A., Kamino, T. & Michael, J. TEM sample preparation and FIB-induced damage. *MRS Bull.* **32**, 401–407 (2007).
52. Volkert, C. A. & Minor, A. M. Focused ion beam microscopy and micromachining. *MRS Bull.* **32**, 389–399 (2007).

53. Dvorak, J., Jarrige, I., Bisogni, V., Coburn, S. & Leonhardt, W. Towards 10 meV resolution: the design of an ultrahigh resolution soft X-ray RIXS spectrometer. *Rev. Sci. Instrum.* **87**, 115109 (2016).
54. Momma, K. & Izumi, F. VESTA: a three-dimensional visualization system for electronic and structural analysis. *J. Appl. Crystallogr.* **41**, 653–658 (2008).

Acknowledgements

This work was supported as part of Programmable Quantum Materials, an Energy Frontier Research Center funded by the US Department of Energy (DOE), Office of Science, Basic Energy Sciences (BES), under award DE-SC0019443. Development of Fe_{4.75}GeTe₂ crystals (AFM) was supported by the U. S. Department of Energy, Office of Science, Basic Energy Sciences, Materials Sciences and Engineering Division. This research used beamlines 2-ID and 4-ID of NSLS-II, a US DOE Office of Science User Facility operated for the DOE Office of Science by Brookhaven National Laboratory under contract no. DE-SC0012704. This research used resources of the Advanced Photon Source, a U.S. Department of Energy (DOE) Office of Science user facility operated for the DOE Office of Science by Argonne National Laboratory under Contract No. DE-AC02-06CH11357.

Author contributions

V.Bi., V.Bh., C.M., A.F.M., D.N.B., and X.X. conceived the research plan. A.F.M. grew and characterized the bulk single-crystalline Fe₅GeTe₂. V.Bi., V.Bh., T.K., J.L., Y.G., S.F., and J.P. carried out the RIXS measurements. V.Bh., T.K., C.M., C.N., and J.W.F. performed the XRD and REXS experiments. T.D. and D.J.R. realized the Raman measurements. V.Bh. and V.Bi. analyzed and interpreted the data, with contributions from all coauthors. V.Bh. and V.Bi. wrote the manuscript. All authors commented on the text.

Competing interests

The authors declare no competing interests.

Additional information

Supplementary information The online version contains supplementary material available at <https://doi.org/10.1038/s41535-025-00803-1>.

Correspondence and requests for materials should be addressed to V. K. Bhartiya or V. Bisogni.

Reprints and permissions information is available at <http://www.nature.com/reprints>

Publisher's note Springer Nature remains neutral with regard to jurisdictional claims in published maps and institutional affiliations.

Open Access This article is licensed under a Creative Commons Attribution-NonCommercial-NoDerivatives 4.0 International License, which permits any non-commercial use, sharing, distribution and reproduction in any medium or format, as long as you give appropriate credit to the original author(s) and the source, provide a link to the Creative Commons licence, and indicate if you modified the licensed material. You do not have permission under this licence to share adapted material derived from this article or parts of it. The images or other third party material in this article are included in the article's Creative Commons licence, unless indicated otherwise in a credit line to the material. If material is not included in the article's Creative Commons licence and your intended use is not permitted by statutory regulation or exceeds the permitted use, you will need to obtain permission directly from the copyright holder. To view a copy of this licence, visit <http://creativecommons.org/licenses/by-nc-nd/4.0/>.

© The Author(s) 2025